

Realizing Thermoelectric and Thermistor Bi-functionalities via Triggering Electron Correlations with Lattice-dipole

Jikun Chen^{1-3†}, Qihao Zhang^{2†}, Jiaou Wang⁴, Jie Xiao², Xinyou Ke⁵, Takeaki Yajima³, Feng Hao²,*

Hongyi Chen², Yong Jiang^{1}, Nuofu Chen⁶ and Lidong Chen^{2*}*

¹Beijing Advanced Innovation Center for Materials Genome Engineering, School of Materials Science and Engineering, University of Science and Technology Beijing, Beijing 100083, China

²State Key Laboratory of High Performance Ceramics and Superfine Microstructure, Shanghai Institute of Ceramics, Chinese Academy of Sciences, Shanghai 200050, China

³School of Engineering, The University of Tokyo, Tokyo 1138656, Japan

⁴Beijing Synchrotron Radiation Facility, Institute of High Energy Physics, Chinese Academy of Sciences, Beijing 100049, China

⁵John A. Paulson School of Engineering and Applied Sciences, Harvard University, Cambridge, Massachusetts 02138, USA

⁶School of Renewable Energy, North China Electric Power University, Beijing 102206, China

Correspondences: Prof. Lidong Chen (cld@mail.sic.ac.cn), Prof. Yong Jiang (yjiang@ustb.edu.cn) and Prof. Jikun Chen (jikunchen@ustb.edu.cn). Request for materials: Prof. Jikun Chen (jikunchen@ustb.edu.cn).

[†]JC and QZ contribute equally to the present work.

Abstract

Establishing strong electron-correlations not only shed lights on overcoming the trade-off limitations for optimizing thermoelectric materials, but can also introduce new functionalities that extend the vision of conventional thermoelectric applications. Here, we demonstrate that the high thermoelectric and thermistor functionalities coexist in lattice distorted $\text{SrNb}_x\text{Ti}_{1-x}\text{O}_3$ films with electron correlations between carriers and ordering aligned lattice dipoles. As-grown $\text{SrNb}_x\text{Ti}_{1-x}\text{O}_3/\text{SrTiO}_3$ with effectively preserved interfacial strains exhibits cross-plane charge ordering and orbital anisotropy, as indicated by the polarization dependent near edge X-ray absorption fine structures. The resultant coulomb-correlations regulate the carrier transport and enhance the Seebeck coefficient more independently via enlarging the system's vibration entropy. As-achieved maximum thermoelectric power factor exceeds $100 \mu\text{Wcm}^{-1}\text{K}^{-2}$ measured in the bulk performance of $\text{SrNb}_{0.2}\text{Ti}_{0.8}\text{O}_3$ ($2.2 \mu\text{m}$)/ SrTiO_3 ($100 \mu\text{m}$), which is comparable to the best thermoelectric materials for low temperature applications. In addition, the strong temperature dependence of the carrier scattering aroused by the lattice dipoles introduces a positive temperature-dependent thermistor transportation behavior with large temperature coefficient of resistance ranging from 30 to 300 K, which is rarely seen in conventional thermistors. Combining both functionalities largely extend the horizon in exploring new Joule sensors for detection of temperature and thermal perturbations across a broad temperature range.

Introduction

Thermoelectric technique can achieve conversions between thermal and electrical energies based on miniaturized and compactly assembled devices, without involving conventional compressors and any mechanical movement.^[1-5] It plays an irreplaceable role in two major aspects: localized refrigeration for microprocessors, and micro-scale power generations from environmental heat.^[1,2] The thermoelectric energy conversion efficiency is determined by a figure of merit, $zT=S^2\sigma T\kappa^{-1}$, of thermoelectric materials (S : Seebeck coefficient, σ : electrical conductivity, T : absolute temperature, and κ : thermal conductivity).^[3,4] Improving zT should follow two directions: reducing lattice contribution in κ , or enhancing thermoelectric power factor ($PF=S^2\sigma$). For Future investigations, it is more urgent and required to achieve further enhancement in PF , since the lattice contribution to κ for many thermoelectric material systems has been reduced towards the amorphous limit within the past two decades^[3-5]. Although PF fundamentally drives the thermoelectric conversion, it is bottlenecked by the reversely varied σ and S with the carrier concentration (n).^[3] How to unlock this conventional S - σ trade-off is one of the most vital issues to be addressed in the field of thermoelectric. Apart from improving zT from the materials aspect, seeking for new applications of the thermoelectric technology is of equal importance. The horizon of thermoelectric will be extended beyond energy conversions, only if additional functionalities can be introduced into the thermoelectric materials to combine with the Seebeck or Peltier effects for achieving new device applications.

Triggering the electron correlations between carriers and ordering aligned array of lattice-dipoles sheds a light on realizing these concepts by breaking through the bottleneck in PF ^[6-18] and meanwhile enriching thermoelectric materials with more functionalities. The past century witnesses the distinct characters discovered in the solid-state matters, such as metal-insulator transitions^[9-13], superconductivities^[14] and bad-metal conductors^[15], via introducing un-negligible coulomb interactions among carriers-carriers and/or carriers-phonons. This was also the case for thermoelectric materials, as we noticed that the electron-phonon coupling (EPC) can cause additional changes in the system entropy associated to the thermal diffusion of carrier, and thereby contribute to an additional Seebeck coefficient (S_{EPC}) that is less dependent on n or σ ^[6-8, 16,17]. One typical example was indicated by an extraordinarily large and n -irrelevant S ($\sim 300 \mu\text{VK}^{-1}$) observed in the heavily doped boron carbides ($\text{B}_{12+x}\text{C}_{3-x}$).^[6-8] The large magnitude of S was mainly contributed by the extra change of entropy when localized carriers coupled with the singlet lattice-dipoles and softened the lattice vibration modes during carrier transport.^[6] Analogous effects were also observed for the two-dimensional electron gas (2DEG) within a $\text{LaAlO}_3/\text{SrTiO}_3$ interfaces^[16,17] or lattice distorted $\text{SrNb}_{0.2}\text{Ti}_{0.8}\text{O}_3/\text{SrTiO}_3$ ^[18], in which cases a large S of $\sim 10^2 \mu\text{VK}^{-1}$ and a high σ of $\sim 10^5 \text{Sm}^{-1}$ coexist as previously attributed to the electron phonon coupling (EPC). These demonstrations indicate an alternative direction to break the S - σ trade-off via actively establishing the EPC, but this has not yet been fully explored compared with the other fields in solid-state matters. Apart from varying the system entropy, the presence of EPC is also expected to strengthen the temperature dependence of the electrical transportations and enhance the

temperature coefficient of resistance (TCR). As a result, an additional functionality of the thermistor transport will be introduced into the thermoelectric material, creating a combined functionality of thermoelectric and thermistor.

In this work, we demonstrate the co-existence of high thermoelectric and thermistor transport performances achieved in lattice distorted $\text{SrNb}_x\text{Ti}_{1-x}\text{O}_3$, by triggering the electron correlations between carriers and the ordering aligned lattice dipoles. The distinct electronic structures of cross-plane ordering and orbital anisotropy were indicated by the polarization dependant near edge X-ray absorption fine structure (NEXAFS). By controlling the lattice mismatch and deposition thickness, we regulated the magnitude of the preserved lattice distortion that is imparted upon $\text{SrNb}_x\text{Ti}_{1-x}\text{O}_3$, and further investigated their relationships with both the thermoelectric and thermistor performances. Potential applications as a Joule sensor for detections of temperature and thermal perturbation are further explored based on the combined functionality of the thermoelectric and thermistor.

Concept

Figure 1a illustrates the general concept to establish an electron - lattice dipole correlated system within niobium doped strontium titanate when binding the distortions induced lattice polarization and interfacial polarization. The strontium titanate is known to exhibit a ferroelectric nature at room temperature when distorted by interfacial strain.^[18-22] Accordingly, a coulomb correlation between carrier and lattice-dipoles will be established by coherently depositing $\text{SrNb}_x\text{Ti}_{1-x}\text{O}_3$ on single-crystal SrTiO_3 substrates under appropriate deposition kinetics. With a larger intrinsic lattice constant than the SrTiO_3 substrate, the co-lattice grown $\text{SrNb}_x\text{Ti}_{1-x}\text{O}_3$ film is under biaxial in-plane compressive distortion, and this is known to separate the charge center of the TiO_6 octahedra and form cross-plane $\text{Ti}^+ \rightarrow \text{O}^-$ lattice-dipoles.^[22] Thermodynamically, as formed lattice-dipoles favored to bind with the interfacial polarization to reach an ordering alignment (\vec{O}) in cross-plane.^[18,27,28] The resultant periodical coulomb potential wells is expected to regulate the carrier distribution and transportations and result in the following two effects.

1) Overcoming S - σ trade-off and improving PF : The S mainly originates from the derivative in the system entropy versus the number of carriers. For conventional thermoelectric materials, S is contributed by the variations in entropy-of-mixing by changing the carrier occupation rate in electronic states (c).^[8] The resultant Seebeck

coefficient resulting for entropy-of-mixing was determined by $S_{\text{mix}} = \left(\frac{k_B}{e}\right) \ln \frac{1-c}{c}$,

where k_B is the Boltzmann constant and c represents the occupation rate of the energy state near the Fermi energy.^[6] Apparently, S_{mix} will increase by reducing carrier concentration (n) and an enhancing density of states (DOS) near the Fermi level^[3], since both ways reduces c and enlarge the entropy change associated to carrier transport driven by temperature gradient. This is also the origin of the conventional S - σ trade-off, since elevating the doping level increases n and σ , but meanwhile

reduces S_{mix} .

By establishing correlations with the lattice-dipoles, per carrier transport induced variation in the system's entropy can be further enlarged via altering the lattice vibration ^[6,7], contributing an extra S_{EPC} to the Seebeck coefficient ($S = S_{EPC} + S_{\text{mix}}$). Treating the vibrations of lattice dipoles are treated as harmonic vibrations at small vibration amplitudes, the S_{EPC} is described as ^[6,7]:

$$S_{EPC} = S_{\text{vibration}} + S_{\text{transport}} = \left(\frac{k_B}{e}\right) \sum_i \left\{ \frac{-\Delta\omega_i}{\omega_i} \left[\frac{\hbar\omega_i / 2k_B T}{\sinh(\hbar\omega_i / 2k_B T)} \right]^2 + \frac{E_{A,i} \hbar\omega_i / 2k_B T}{\sinh(\hbar\omega_i / 2k_B T)} \right\} \quad (1)$$

Where, the $\Delta\omega_i$ represents the changes in vibration frequency associated to coupling with carriers at each vibration frequency of ω_i , $E_{A,i}$ is the activation energy for carrier transportation at ω_i , k_B is the Boltzmann constant and \hbar is the reduced Planck constant. As indicated by Eq. (1), S_{EPC} is mainly determined by the number of coupled frequency between electron and phonons, and the respective magnitude of $\Delta\omega_i$ and $E_{A,i}$ at each frequency. This indicates the two keys to achieve large S_{EPC} : strengthening the strain-induced lattice polarization and enhancing their couplings.

2) Introducing thermistor transportations with large TCR: The vibrations of lattice dipoles are usually activated by phonons, and their further coupling with the carrier transport is expected to strengthen the temperature dependence of the resistivity. For example, elevating the temperature will promote the vibrations of the lattice dipoles that result in more significantly carrier scatterings, as compared to conventional semiconductors. Therefore, a more dramatic enhancement in the resistivity of the material is expected, achieving a thermistor transportation behavior with a relatively large positive TCR. This concept was confirmed by the observed large positive temperature dependence in the 2DEGs within LaAlO₃/SrTiO₃ interfaces ^[16,17], in which case the electron carriers underneath the interface correlated with the interfacial polarizations that are perpendicular to the carrier transport. Compared with the LaAlO₃/SrTiO₃, as-proposed lattice distorted SrNb_xTi_{1-x}O₃/SrTiO₃ exhibits a similar electronic structure and the way in carrier transportation. For example, interfacial polarization at SrNb_xTi_{1-x}O₃/SrTiO₃ can be considered to be effectively extended within the SrNb_xTi_{1-x}O₃ film materials, resulting in a thermistor transportation behavior.

The thermistor transport functionality was applied previously in aspects such as a Joule sensor for detections of temperature and/or thermal perturbation, circuit protection and current limiting, and temperature compensated synthesizer voltage controlled oscillators ^[39-41]. Nevertheless, one challenge in Joule sensing is the relative small magnitude of TCR (i.e. $\sim 1-2 \%$ K⁻¹) of conventional thermistors, resulting in relatively small magnitude of the reading out voltage signal compared to the background signal introduced by the input electric current signal at a small temperature raise. Compared to Joule sensing via thermistor, the Seebeck effect in thermoelectric functionality provides another direction to sense the incident Joule heat via its resultant temperature difference. This process does utilize any input electronic signals that easily enhances the background signal, but requires a reaction time to

establish a temperature gradient that further generates the Seebeck voltage to be read out. Therefore, a larger tolerance in compromising between high detection resolution and fast reaction speed is expected in a new Joule sensor combining both the thermoelectric and thermistor functionalities.

Results and discussions

To achieve as-proposed concept and further regulate both thermoelectric and thermistor transport functionalities, we adjust the lattice constant (a_0) and deposition thickness (t_{Film}) of the films growing on SrTiO₃ (001) substrate to control the preservation of interfacial strain and its induced lattice polarization. For example, single-layer SrNb_{0.2}Ti_{0.8}O₃ or SrNb_{0.4}Ti_{0.6}O₃ were deposited at various t_{Film} on SrTiO₃ (001). In addition, laminated layers, such as SrNb_{0.4}Ti_{0.6}O₃ /SrNb_{0.2}Ti_{0.8}O₃ and SrNb_{0.4}Ti_{0.6}O₃ /SrNb_{0.2}Ti_{0.8}O₃, at a similar t_{Film} were also deposited on SrTiO₃ (001). The SrNb_{0.2}Ti_{0.8}O₃ ($a_0= 3.96$ Å) exhibits a smaller lattice mismatch ($\epsilon=1.42\%$) with the SrTiO₃ ($a_0= 3.905$ Å) substrate, compared to the ones for SrNb_{0.4}Ti_{0.6}O₃ ($a_0= 4.00$ Å) with SrTiO₃ ($\epsilon=2.55$ %). As a result, a better coherency in the epitaxy was observed when depositing SrNb_{0.2}Ti_{0.8}O₃ compared with SrNb_{0.4}Ti_{0.6}O₃. This is further indicated by the reflection high-energy electron diffraction results (see Figure S1 with more discussions in SI: section C).

The lattice distortions of the film material are quantified from reciprocal space mappings (RSM), as shown in Figure 1b for four representative films at similar deposition thicknesses. Their X-ray diffraction (XRD) patterns are demonstrated in Figure S2. In the RSM spectrums, $I_{Film(Q//,Q\perp)}$ and $I_{Substr.(Q//,Q\perp)}$, represent the material diffractions distributed at the in-plane ($Q//$) and cross-plane ($Q\perp$) reciprocal coordinate, respectively. Accordingly, the averaged biaxial lattice distortion and the percentage of materials distributed in each magnitude of lattice distortion were calculated^[18]. For single layered films at a similar deposition thickness, the lattice compression is more preserved for the SrNb_{0.2}Ti_{0.8}O₃/SrTiO₃, compared to SrNb_{0.4}Ti_{0.6}O₃/SrTiO₃ (see the strain distributions in Figure 1b). For laminated layered films, the sequence of layer lamination can also influence the preservation of lattice distortions, since the strain relaxes differently at various ϵ . This is seen from the better preserved lattice distortion for SrNb_{0.4}Ti_{0.6}O₃/SrNb_{0.2}Ti_{0.8}O₃/SrTiO₃, compared to SrNb_{0.4}Ti_{0.6}O₃/SrNb_{0.2}Ti_{0.8}O₃/SrTiO₃.

The interfacial strain induce compressive lattice distortion is expected to further influence the electronic structures and charge ordering of as-grown film material. Therefore, the polarization dependent near edge X-ray absorption fine structures (NEXAFS)^[29-31] were performed for SrNb_{0.2}Ti_{0.8}O₃ (400 nm)/SrTiO₃, SrNb_{0.2}Ti_{0.8}O₃ (400 nm)/LaAlO₃, SrNb_{0.4}Ti_{0.6}O₃ (400 nm)/SrTiO₃ and SrTiO₃ single crystal, as the results shown in Figure 1c. Since the depth in response of the X-ray absorption was around 100 nm, as-obtained signal is from the film material.^[29] The conduction band splits into four energy levels, among which the two lower energy orbits of t_{2g} and e_g originate from O-2*p* hybridized with Ti-3*d* orbits.^[32-34] The undistorted or strain relaxed SrTiO₃ (or SrNb_xTi_{1-x}O₃) exhibits an octahedral symmetry (TiO₆), in which case the e_g orbits from hybridization between O-2*p* and Ti-3*d* are expected to be

isotropy for the in-plane and cross-plane directions. This is in agreement with the non-angular dependent NEXAFS spectrums observed for the undistorted SrTiO₃ single crystals (Figure S3), the strain-relaxed SrNb_{0.2}Ti_{0.8}O₃/LaAlO₃ (Figure 1c, middle), and partially strain-relaxed and SrNb_{0.4}Ti_{0.6}O₃/SrTiO₃ (Figure 1c, right).

In contrast, a polarization dependent e_g orbit is observed for SrNb_{0.2}Ti_{0.8}O₃/SrTiO₃ (Figure 1c, left), indicating a strong orbital anisotropy in the σ -bond hybridized by O-2p (σ) hybridized with Ti-3d. An enhanced resonance is observed when the electric field from the polarized X-ray exhibits smaller angle with respect to the cross-plane direction. This is in consistency with the resonance of electrons in the dipole approximation with the linearly polarized X-ray from synchrotron radiations, as described previously to be ^[29]: $I \propto \left| \langle \psi_f | e \cdot p | \psi_i \rangle \right|^2 \propto \left| \vec{E} \cdot \vec{O} \right|^2$. The term $\left| \langle \psi_f | e \cdot p | \psi_i \rangle \right|^2$ determines the magnitude of resonance cross-section and is proportional to the absorption intensity (I), where Ψ_f and Ψ_i represent the final and initial state, e is the unit electric field vector, and p is the dipole transition operator.

Similar phenomenon was previously observed in ferroelectric or magnetic domains of materials, such as BiFeO₃^[30] and FeTiO₃^[31]. For the present SrNb_{0.2}Ti_{0.8}O₃/SrTiO₃, the aligned Ti⁺→O⁻ lattice-dipoles and their influence in the distribution of electron carriers along the cross-plane direction are expected to form an ordering and directional polarization state (\vec{O}). The resonance is maximized when \vec{O} is along the electromagnetic field of the polarized X-ray (\vec{E}) and minimized when \vec{O} is perpendicular to \vec{E} .^[29-32] It is also interesting to note that compared with SrNb_{0.2}Ti_{0.8}O₃/LaAlO₃, the relative absorption intensity for the e_g orbit is lower for SrNb_{0.2}Ti_{0.8}O₃/SrTiO₃, in particular along the cross-plane direction. This indicates a reduced proportion of DOS hybridized from O-2p in the conduction band, and should be associated to the enhanced coulomb repulsion between the lattice-dipoles regulated in-plane electron carriers with their adjacent oxygen sites.

The orderly alignment in the charge anisotropic lattice-dipoles in SrNb_{0.2}Ti_{0.8}O₃/SrTiO₃ is expected to zigzag the previous conduction band owing to their respective impact on the carrier distributions and transportations^[15,16,18,24]. In Figure 2a, the S and deposition induced sheet conductance (σ_{xx}/t_{Film}) measured at room temperature are compared for as-grown SrNb_xTi_{1-x}O₃ at various magnitudes of lattice distortions. In general, both the S and σ_{xx}/t_{Film} for SrNb_xTi_{1-x}O₃/SrTiO₃ shows an increasing tendency with an enlarged lattice distortion. In contrast, the SrNb_xTi_{1-x}O₃/LaAlO₃ and SrNb_xTi_{1-x}O₃/(LaAlO₃)_{0.3}(Sr₂AlTaO₆)_{0.7} with completely relaxed interfacial strains (see RSM spectrum in Figure S4) exhibits a similar S and σ_{xx}/t_{Film} to their respective bulk values at similar compositions. The deposition induced carrier density and carrier mobility were further shown in Figure S5 for several representative samples. When growing on LaAlO₃ substrate to relax the interfacial strains, a larger carrier density (Figure S5a) and smaller mobility (Figure S5b) is

observed for $\text{SrNb}_{0.4}\text{Ti}_{0.6}\text{O}_3$ as compared to $\text{SrNb}_{0.2}\text{Ti}_{0.8}\text{O}_3$. This tendency is in agreement to the conventional thermoelectric bulk materials, when increasing the doping concentration. When growing on the SrTiO_3 substrate, both the carrier density (Figure 5c) and mobility (Figure 5d) enhances with the magnitude of the preserved lattice distortions. This observation reveals that the carrier formation and transportation for the presently grown $\text{SrNb}_x\text{Ti}_{1-x}\text{O}_3/\text{SrTiO}_3$ is more dominated by the lattice distortion or polarization rather than element doping, and this differs from conventional thermoelectric materials.

The above understanding is further supported by comparing the temperature dependence in the electrical transportation properties. As shown Figure 2b, the sheet resistance (R_{xx}) for the strain relaxed $\text{SrNb}_x\text{Ti}_{1-x}\text{O}_3/\text{LaAlO}_3$ remains nearly constant when varying the temperature (T), and this is similar to the tendency observed for heavily doped $\text{SrNb}_x\text{Ti}_{1-x}\text{O}_3$ bulk materials. In contrast, the $\text{SrNb}_x\text{Ti}_{1-x}\text{O}_3/\text{SrTiO}_3$, which exhibits a thermistor transportation behaviour with steeply increasing R_{xx} - T tendencies across a broad range of temperature from 10 to 300 K. Elevating the temperature results in a reduction of their TCR reduces from a magnitudes of $\sim 5\% \text{ K}^{-1}$ at 10 K to $\sim 1\% \text{ K}^{-1}$ at 300 K. A further comparison indicates a larger TCR near room temperature is observed for more distorted samples, e.g. $\text{SrNb}_{0.2}\text{Ti}_{0.8}\text{O}_3/\text{SrTiO}_3$ compared to $\text{SrNb}_{0.4}\text{Ti}_{0.6}\text{O}_3/\text{SrTiO}_3$.

To better understand the R_{xx} - T tendencies, Hall measurement was performed to investigate the temperature dependence of the sheet carrier density ($n_{xx}=R_{\text{Hall}}^{-1}$) and carrier mobility (μ_{Hall}), as their results demonstrated in Figure 2c. A nearly constant n_{xx} is observed for $\text{SrNb}_{0.2}\text{Ti}_{0.8}\text{O}_3/\text{SrTiO}_3$, $\text{SrNb}_{0.4}\text{Ti}_{0.6}\text{O}_3/\text{SrNb}_{0.2}\text{Ti}_{0.8}\text{O}_3/\text{SrTiO}_3$, and $\text{SrNb}_{0.2}\text{Ti}_{0.8}\text{O}_3/\text{LaAlO}_3$, in which situations the interfacial strain either preserved or completely relaxed. For strain partially relaxed samples, such as $\text{SrNb}_{0.4}\text{Ti}_{0.6}\text{O}_3/\text{SrTiO}_3$ and $\text{SrNb}_{0.2}\text{Ti}_{0.8}\text{O}_3/\text{SrNb}_{0.4}\text{Ti}_{0.6}\text{O}_3/\text{SrTiO}_3$, elevating T results in a more significant enhancement in their n_{xx} . This may associate to the thermal activation of carriers that were previously trapped by the lattice defects within the strain gradual relaxation region. The $\mu_{\text{Hall}}-T$ observed for $\text{SrNb}_x\text{Ti}_{1-x}\text{O}_3/\text{SrTiO}_3$ exhibits a significantly reducing tendencies similar to the previously reported ones for the 2DEGs within the $\text{LaAlO}_3/\text{SrTiO}_3$ interfaces^[16,17], and in contrast to the constant $\mu_{\text{Hall}}-T$ tendency observed for $\text{SrNb}_{0.2}\text{Ti}_{0.8}\text{O}_3/\text{LaAlO}_3$.

To further cater to practical applications in thermoelectric energy conversions, the deposition thickness (t_{Film}) was increased beyond a micrometer-scale, and meanwhile the thickness of the SrTiO_3 (001) substrates ($t_{\text{Substrate}}$) was reduced to 100 μm . Four representative $\text{SrNb}_x\text{Ti}_{1-x}\text{O}_3$ (1.2-2.8 μm) / SrTiO_3 (100 μm) samples were prepared under the same deposition condition for the present investigation. Owing to a smaller lattice mismatch, as-deposited $\text{SrNb}_{0.2}\text{Ti}_{0.8}\text{O}_3/\text{SrTiO}_3$ (sample A and B) and $\text{SrNb}_{0.1}\text{Ti}_{0.9}\text{O}_3/\text{SrTiO}_3$ (sample D) are more distorted compared with the $\text{SrNb}_{0.4}\text{Ti}_{0.6}\text{O}_3/\text{SrTiO}_3$ (sample C), as shown in Figure S6. Figure 3a shows the temperature dependent S and σ for four samples, measured as a bulk material by integrating the thickness of both films and substrates where $\sigma=\sigma_{xx}(t_{\text{Film}}+t_{\text{Substrate}})^{-1}$. At room temperature, sample C exhibits a similar Seebeck coefficient to the bulk value of $\text{SrNb}_{0.4}\text{Ti}_{0.6}\text{O}_3$, while its sheet conductance ($\sigma_{xx} = 0.47 \text{ } \Omega^{-1} \text{ sq.}$) is similar to a 1.6

μm thick $\text{SrNb}_{0.4}\text{Ti}_{0.6}\text{O}_3$ bulk layer ($\sigma_{xx} = 0.41 \Omega^{-1} \text{sq.}$). In contrast, the sheet resistance for sample A, B and D are around three times larger than the ones from their respective bulk layers at the same thicknesses. Compared with the strain-relaxed $\text{SrNb}_{0.4}\text{Ti}_{0.6}\text{O}_3/\text{SrTiO}_3$ (Sample C), the distorted $\text{SrNb}_{0.2}\text{Ti}_{0.8}\text{O}_3/\text{SrTiO}_3$ (Sample A and B) and $\text{SrNb}_{0.1}\text{Ti}_{0.9}\text{O}_3/\text{SrTiO}_3$ (Sample D) exhibit larger S and σ over all the measured temperature range of 10-300 K. These results are consistent with the ones observed in Figure 2a. Comparing the performance of Sample A and B with different t_{Film} , the sheet conductance shows a linear enhancement with the thin film deposition thickness as demonstrated in Figure S7. We can further estimate the additional introduced conductance and Seebeck coefficient by increasing the deposition thickness of $1.6 \mu\text{m}$, via $\sigma_{1.6\mu\text{m}} = (\sigma_{xx,B} - \sigma_{xx,A})(t_B - t_A)^{-1}$ and $S_{1.6\mu\text{m}} = (S_B \sigma_{xx,B} - S_A \sigma_{xx,A})(\sigma_{xx,B} - \sigma_{xx,A})^{-1}$, respectively, as shown in Figure S8.

In Figure 3b, we further compare the thermoelectric power factor (PF) for the Sample A and B with the reported thermoelectric materials^[35-38]. It can be seen that the presently achieved maximum PF when treating the $\text{SrNb}_{0.2}\text{Ti}_{0.8}\text{O}_3$ ($2.8 \mu\text{m}$)/ SrTiO_3 ($100 \mu\text{m}$) sample as bulk material (by considering the sum of thicknesses for the film and substrate) is approaching to the one observed in $\text{Bi}_{1-x}\text{Sb}_x$ at low temperature range. The dash-line in Figure 3b shows the calculated magnitude for using $S_{1.6\mu\text{m}}^2 \sigma_{1.6\mu\text{m}}$, indicating the introduced PF by depositing additional $1.6 \mu\text{m}$ film material. By either calculating the κ_{Film} from as measured $\kappa_{\text{Film\&Substrate}}$ (Figure S9a) or performing similar estimation to ref [24], the obtained κ_{Film} is in the magnitude of $\sim 13\text{-}15 \text{ Wm}^{-1}\text{K}^{-1}$ (Figure S9b). More details of the two approaches for calculating the κ_{Film} are demonstrated in the supporting information (Figure S9). The resultant zT values associated to the film materials at room temperature for sample A-C are estimated to be of ~ 0.8 to 1.0 (Figure S9c), a room temperature performance comparable to $\text{Bi}_2\text{Se}_0.3\text{Te}_{2.7}$ ^[4]. By further reducing the temperature, the low temperature zT values achieved presently are expected to exceed the reported ones from the best low temperature thermoelectric materials such as $\text{Bi}_{1-x}\text{Sb}_x$ ^[36] and CsBi_4Te_6 ^[37] as demonstrated in Figure S9d.

The enhancement in thermoelectric performances is expected to be associated to the unlocked S - σ inter-relations when actively triggered carriers coulomb correlations with the orderly aligned cross-plane array of the lattice dipoles. In Figure 3c, the S - σ tendency at room temperature for samples in this work are compared with the reported ones for bulk or 2DEG-related SrTiO_3 ^[24-26], as well as the typical thermoelectric materials used near room temperature or below.^[35-37] The film materials of $\text{SrNb}_{0.2}\text{Ti}_{0.8}\text{O}_3$ and $\text{SrNb}_{0.1}\text{Ti}_{0.9}\text{O}_3$ in this work exhibit a large S of $\sim 320 \mu\text{VK}^{-1}$ at a relatively high electrical conductivity of $\sim 4.5 \times 10^5 \text{ Sm}^{-1}$. Their respective S - σ relations at room temperature follow ones observed for the SrTiO_3 -related 2DEGs.^[24,25] In contrast, the S - σ relation of the strain-relaxed $\text{SrNb}_{0.4}\text{Ti}_{0.6}\text{O}_3$ film material follows the doped- SrTiO_3 as a bulk material. This is in agreement to the NEXAFS results demonstrated in Figure 1c, since an ordering aligned lattice polarization structure along the cross-plane direction is expected to form periodical well-like potentials. This results in more centralized spatial distribution of the carriers within the potential-well and forms a multi-channel quasi-2D transportations, similar

to the ones observed for superlattice or interfacial 2DEGs.

Combining both functionalities of high thermoelectric and thermistor transportation can extend the vision in further exploring new applications of the thermoelectric materials apart from conventional thermoelectric energy conversions. One example demonstrated in Figure 4 is to achieve broad-range temperature sensing and imaging the localized thermal perturbation based on both functionalities of the presently grown $\text{SrNb}_x\text{Ti}_{1-x}\text{O}_3/\text{SrTiO}_3$. Figure 4a demonstrates the flow chart of the detection strategy. The film material can be manufactured into the T-shape and aligned in an array, in which situation the thermistor and thermoelectric functionalities are used along the transverse and longitudinal ways, respectively. Under a given environment, the temperature can be detected via the R_{xx} - T tendency, as one example given in Figure 4b and S10.

When knowing the temperature, the device can be further used for sensing or imaging the thermal perturbation via two modes: 1) the fast response mode based on the functionality of thermistor; 2) the high resolution based on the functionality of thermoelectric. We further performed the finite element simulation on the detection prototype to compare the two different modes in Joule detections via thermistor and thermoelectric functionalities, the results of which are detailed in Figure S10. As a thermal perturbation is applied onto the crossing point, the raised temperature (ΔT) in localized region can be fast sensed via the enhancement in the transverse resistance (R_T). This can be detected by applying a transverse current I_0 and the change of transverse voltage (V_R) can be sensed as $V_R/V_{R0} = (1 + \text{TCR}\Delta T)$. Meanwhile, the magnitude of ΔT can be better resolved via its resultant Seebeck voltage ($V_s = S\Delta T$) in longitudinal way via the thermoelectric functionality, utilizing the large magnitude of S ($\sim 10^2 \mu\text{V K}^{-1}$). Figure 4c demonstrates the temperature dependence of the TCR and S for the present $\text{SrNb}_x\text{Ti}_{1-x}\text{O}_3/\text{SrTiO}_3$ (100 μm) samples in comparison with the ones for BiSb, which is the most commonly used thermoelectric materials in the low temperature range. It can be seen that within a broad temperature range from 70 K to room temperature, both the TCR and S of the $\text{SrNb}_x\text{Ti}_{1-x}\text{O}_3/\text{SrTiO}_3$ far exceeds the ones observed for the conventional low temperature thermoelectric material of BiSb [36].

Conclusion

In summary, both functionalities of high thermoelectric and thermistor transportation were achieved in lattice distorted $\text{SrNb}_x\text{Ti}_{1-x}\text{O}_3$ via triggering the coulomb correlations between the carrier and ordering aligned lattice dipoles. Binding the strain induced lattice polarization with the interfacial polarization results in ordering alignment of the cross-plane $\text{Ti}^+ \rightarrow \text{O}^-$ lattice-dipoles that couples with the carrier transport, as indicated by polarization dependent NEXAF analysis. As a result, the change of entropy from softening the phonon mode was enhanced that introduces an additional S_{EPC} to break the conventional S - σ trade-off and further improve the thermoelectric performances. Even considering the film and substrate as a bulk material, the maximum PF of the $\text{SrNb}_{0.2}\text{Ti}_{0.8}\text{O}_3$ (2.8 μm)/ SrTiO_3 (100 μm) sample reaches to $\sim 103 \mu\text{Wcm}^{-1}\text{K}^{-2}$ at 45 K. This should be the highest PF ever reported for

thermoelectric oxides as bulk materials and approaches the ones for the best report from $\text{Bi}_{1-x}\text{Sb}_x$ at low temperatures. In addition to the thermoelectric functionality, a thermistor transportation behavior with large TCR across a broad temperature range was achieved in as-grown lattice distorted $\text{SrNb}_x\text{Ti}_{1-x}\text{O}_3/\text{SrTiO}_3$, owing to the temperature dependence of the carrier scattering by the lattice dipoles. Combining both functionalities of thermoelectric and thermistor transportation will largely extend the vision in designing new electronic devices and exploring their new applications in aspects such as Joule sensor for detections of the temperature and thermal perturbations.

References

- [1] A. Majumdar, Thermoelectric devices: Helping chips to keep their cool. *Nat. Nanotechnol.*, **2009**, 4, 214-215
- [2] Venkatasubramanian, R.; Siivola, E.; Colpitts, T.; O'Quinn, B. Thin-film thermoelectric devices with high room-temperature figures of merit. *Science*, **2001**, 413, 597-602
- [3] Dresselhaus, M. S.; Chen, G.; Tang, M. Y.; Yang, R. G.; Lee, H.; Wang, D. Z.; Ren, Z. F.; Fleurial Z. P.; Gogna, P. Fleurial Z. P.; *et al.* New directions for low-dimensional thermoelectric materials. *Adv. Mater.*, **2007**, 19, 1043-1053
- [4] Zhu, T.; Liu, Y.; Fu, C.; Heremans, J. P.; Snyder, J. G.; Zhao, X. Compromise and synergy in high-efficiency thermoelectric materials. *Adv. Mater.*, **2017**, 29, 1605884
- [5] Pei, Y. Z.; Shi, X. Y.; LaLonde, A.; Wang, H.; Chen, L. D.; Snyder, G. J. Convergence of electronic bands for high performance bulk thermoelectrics. *Nature*, **2011**, 473, 66-69
- [6] Emin, D. Enhanced Seebeck coefficient from carrier-induced vibrational softening. *Phys. Rev. B*, **1999**, 59, 6205-6210
- [7] Aselage, T. L.; Emin, D.; McCready, S. S.; Duncan, R. V. Large Enhancement of Boron Carbides' Seebeck Coefficients through Vibrational Softening. *Phys. Rev. Lett.* **1998**, 81, 2316-2319.
- [8] Koshibae, W.; Tsutsui, K.; Maekawa, S. Thermopower in cobalt oxides. *Phys. Rev. B*, **2000**, 62, 6869-6872
- [9] Dagotto, E. complexity in strongly correlated electronic systems. *Science*, **2005**, 309, 257
- [10] Gruner, G. The dynamics of charge-density waves. *Rev. Mod. Phys.*, **1988**, 60, 1129-1182
- [11] Zettl, A.; Gruner, G. Onset of charge-density-wave conduction: Switching and hysteresis in

NbSe₃. *Phys. Rev B*, **1982**, 26, 2298-2301

[12] Mott, N. F. Metal-insulator transition. *Rev. Mod. Phys.*, **1968**, 40, 677-783

[13] Imada, M.; Fujimori, A.; Tokura, Y.; metal-insulator transitions. *Rev. Mod. Phys.*, **1988**, 70, 1039

[14] Dagotto, E.; Correlated electrons in high-temperature superconductors. *Rev. Mod. Phys.*, **1994**, 66, 763

[15] R. Jaramillo, Sieu D. Ha, D. M. Silevitch and Shriram Ramanathan, Origins of bad-metal conductivity and the insulator-metal transition in the rare-earth nickelates. *Nat. Phys.*, **2014**, 10, 304

[16] Pallecchi, I.; Telesio, F.; Marré, D.; Li, D.; Gariglio, S.; Triscone, J. M.; Filippetti, A. Large phonon-drag enhancement induced by narrow quantum confinement at the LaAlO₃/SrTiO₃ interface. *Phys. Rev. B*, **2016**, 93, 195309

[17] Pallecchi, I.; Telesio, F.; Li, D. F.; Fête, A.; Gariglio, S.; Triscone, J. M.; Filippetti, A.; Delugas, P.; Fiorentini, V.; Marré, D. Giant oscillating thermopower at oxide interfaces. *Nat. Commun.* **2015**, 6, 6678

[18] Chen, J.; Chen, H.; Hao, F.; Ke, X.; Chen, N.; Yajima, T.; Jiang, Y.; Shi, X.; Zhou, K.; Döbeli, M.; Zhang, T.; Ge, B.; Dong, H.; Zeng, H.; Wu, W.; Chen, L. Ultrahigh thermoelectric performance in SrNb_{0.2}Ti_{0.8}O₃ oxide films at a submicrometer-scale thickness. *ACS Energy Lett.*, **2017**, 2, 915-921

[19] Streiffner, S. K.; Chen, L. Q.; Kirchoefer, S. W.; Levy, J.; Schlom, D. G. Room-temperature ferroelectricity in strained SrTiO₃. *Nature*, **2004**, 403, 758-761

[20] Haeni, J. H.; Irvin, P.; Chang, W.; Uecker, R.; Reiche, P.; Li, Y. L.; Choudhury, S.; Tian, W.; Hawley, M. E.; Craigo, *et al.* Stress-induced ferroelectricity and soft phonon modes in SrTiO₃. *Phys. Rev. B*, **1976**, 13, 271-286

[21] Pertsev, N. A.; Tagantsev, A. K.; Setter, N. Phase transitions and strain-induced ferroelectricity in SrTiO₃ epitaxial thin films. *Phys. Rev. B*, **2000**, 61, R825

[22] Verma, A.; Raghavan, S.; Stemmer, S.; Jena, D. Ferroelectric transition in compressively strained SrTiO₃ thin films. *Appl. Phys. Lett.*, **2015**, 107, 192908

[23] Cain, T. A.; Kajdos, A. P.; Stemmer, S. La-doped SrTiO₃ films with large cryogenic thermoelectric power factors. *Appl. Phys. Lett.*, **2013**, 102, 182101

[24] Ohta, H.; Kim, S.; Mune, Y.; Mizoguchi, T.; Nomura, K.; Ohta, S.; Nomura, T.; Nakanishi, Y.;

Ikuhara, Y.; Hirano, M.; *et al.* Giant thermoelectric Seebeck coefficient of a two-dimensional electron gas in SrTiO₃. *Nat. Mater.*, **2007**, 6, 129-134

[25] Ohta, H.; Sugiura, K.; Koumoto, K. Recent progress in oxide thermoelectric materials: p-type Ca₃Co₄O₉ and n-type SrTiO₃. *Inorg. Chem.*, **2008**, 47, 8429-8436

[26] Okuda, T.; Nakanishi, K.; Miyasaka, S.; Tokura, Y. Large thermoelectric response of metallic perovskites: Sr_{1-x}La_xTiO₃ (0 ≤ x ≤ 0.1). *Phys. Rev. B*, **2001**, 63, 113104

[27] Ambacher, O.; Smart, J.; Shealy, J. R.; Weimann, N. G.; Chu, K.; Murphy, M.; Schaff, W. J.; Esatman, L. F.; Dimitrov, R.; Witt, L.; *et al.* Two-dimensional electron gases induced by spontaneous and piezoelectric polarization charges in N- and Ga-face AlGaIn/GaN heterostructures. *J. Appl. Phys.*, **1999**, 85, 3222-3233

[28] Ibbetson, J. P.; Finil, P. T.; Ness, K. D.; Denbaars, S. P.; Speck, J. S.; Mishra, U. K. Polarization effects, surface states, and the source of electrons in AlGaIn/GaN heterostructure field effect transistors. *Appl. Phys. Lett.*, **2000**, 77, 250-252

[29] Hähner, G. Near edge X-ray absorption fine structure spectroscopy as a tool to probe electronic and structural properties of thin organic films and liquids. *Chem. Soc. Rev.*, **2006**, 35, 1244

[30] Ko, K. T.; Jung, M. H.; He, Q.; Lee, J. H.; Woo, C. S.; Chu, K.; Seidel, J.; Jeon, B. G.; Oh, Y. S.; Kim, K. H.; Liang, W.; Chen, H. J.; Chu, Y. H.; Jeong, Y. H.; Ramesh, R.; Park, J. H.; Yang, C. H. Concurrent transition of ferroelectric and magnetic ordering near room temperature. *Nat. Comm.*, **2011**, 2, 567

[31] Haw, S. C.; Lee, J. M.; Chen, S. A.; Lu, K. T.; Lin, P. A.; Lee, C. H.; Lee, M. T.; Pi, W. P.; Hu, Z.; Chen, J. M. Anisotropic orbital occupation and Jahn-Teller distortion of orthorhombic YMnO₃ epitaxial films: A combined experimental and theoretical study on polarization dependent x-ray absorption spectroscopy. *J. Chem. Phys.*, **2014**, 140, 154503

[32] See, A. K.; Thayer, M.; Bartynski, R. A. Angle-resolved inverse-photoemission study of the nearly perfect TiO₂(110) surface. *Phys. Rev. B*, **1993**, 47, 13722-13729

[33] Tokura, Y.; Nagaosa, N. Orbital physics in transition-metal oxides. *Science*, **2000**, 288, 462

[34] de Groot, F. M. F.; Faber, J.; Michiels, J. J. M.; Czyiyk, M. T.; Abbate, M.; Fuggle, J. C. Oxygen 1s x-ray absorption of tetravalent titanium oxides: a comparison with single-particle calculations. *Phys. Rev. B*, **1993**, 48, 2074

[35] Hu, L.; Wu, H.; Zhu, T.; Fu, C.; He, J.; Ying, P.; Zhao, X. Tuning multiscale microstructures to enhance thermoelectric performance of n-Type bismuth telluride based solid solutions. *Adv. Energy Mater.*, **2015**, 5, 1500411

- [36] Lenoir, B.; Dauscher, A.; Cassart, M.; Ravich, Y. I.; Scherrer, H. Effect of antimony content on the thermoelectric figure of merit of $\text{Bi}_{1-x}\text{Sb}_x$ alloys. *Phys. Chem. Solid*, **1998**, 59, 129-134
- [37] Chung, D. Y.; Hogan, T.; Brazis, P.; Rocci-Lane, M.; Kannewurf, C.; Bastea, M.; Uher, C.; Kanatzidis, M. G. CsBi_4Te_6 : A high-performance thermoelectric material for low-temperature applications. *Science*, **2000**, 287, 1024-1027
- [38] Bentien, A.; Johnsen, S.; Madsen, G. K. H.; Iversen, B. B.; Steglich, F. Colossal Seebeck coefficient in strongly correlated semiconductor FeSb_2 . *Europhy. Lett.*, **2007**, 80, 17008
- [39] Ohg, E. Negative temperature coefficient resistance (NTCR) ceramic thermistors: an industrial perspective. *J. Am. Ceram. Soc.* **2009**, 92[5] 967–983
- [40] Rogalski, A. Infrared detectors: an overview. *Infrared Physics & Technology* **2002**, 43, 187–210
- [41] Li, Z.; Hu, Z.; Peng, J.; Wu, C.; Yang, Y.; Feng, F.; Gao, P.; Yang, J.; Xie, Y. Ultrahigh infrared photoresponse from core-shell single domain- $\text{VO}_2/\text{V}_2\text{O}_5$ heterostructure in nanobeam. *Adv. Funct. Mater.* **2014**, 24, 1821–1830

Acknowledgments

This work is supported by the National Natural Science Foundation of China (No. 51602022, No. 61674013 and No. 1157227), the key research program of Chinese Academy of Sciences (Grant No. KGZD-EW-T06) and the research grant from Shanghai government (No. 15JC1400301). JC also appreciate Japanese Society for the Promotion of Science (Fellowship ID: P15363). We appreciate helpful discussions and technical supports by Prof. Akira Toriumi from The University of Tokyo (Japan), Dr. Guolei Xiang from University of Cambridge (United Kingdom) and Prof. Renkui Zheng from Shanghai Institute of Ceramics, Chinese Academy of Sciences (China).

Competing Interests: The authors declare no competing financial interest.

Additional Information: Supplementary Information is available for this manuscript.

Correspondences: Correspondences should be addressed to: Prof. Lidong Chen (cld@mail.sic.ac.cn), Prof. Yong Jiang (yjiang@ustb.edu.cn) and Prof. Jikun Chen (jikunchen@ustb.edu.cn). Request for materials should contact Prof. Jikun Chen (jikunchen@ustb.edu.cn).

Author Contributions: JC conceived the idea, planned for the experiments, developed the film deposition strategy, performed film growth, and wrote the manuscript assisted by LC and QZ; QZ performed the simulation; JW and JC managed the synchrotron experiment and data analysis; JX, HC and FH characterized the transportation performance; JC and XK contributed to the RSM measurement and analysis; JC, YT, NC and YJ provided experimental supports and useful discussions.

Figures and Captions:

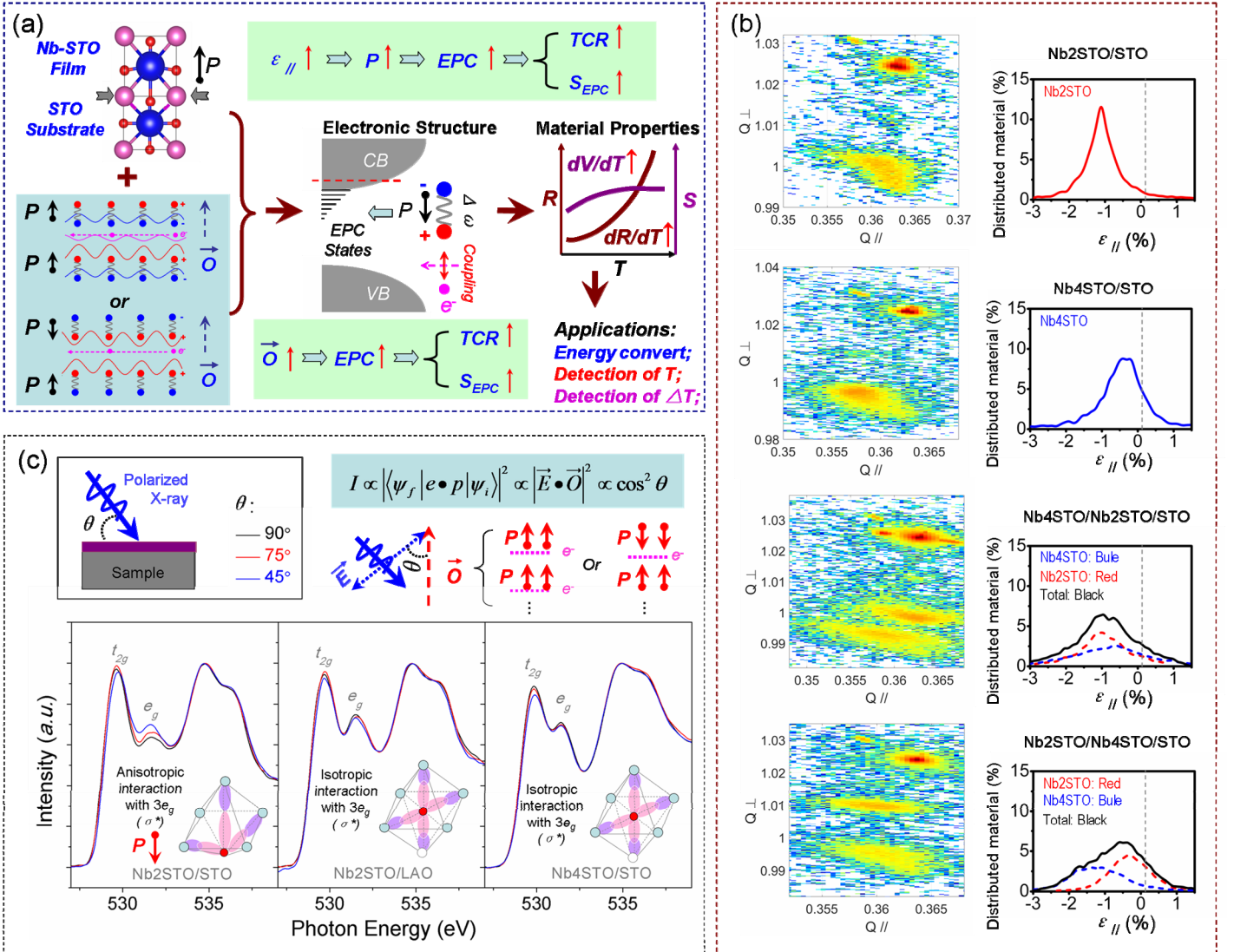


Figure 1. (a) Schematic illustration of a concept to enhance the Seebeck coefficient by coupling the cross-plane ordering aligned ferroelectric polarons and electron carriers, and meanwhile establishing the thermistor transportation functionality. (b) Reciprocal space mapping (RSM) and the percentage of material distributed as a function of the lattice distortions for: SrNb_{0.2}Ti_{0.8}O₃ ($t = 440$ nm) / SrTiO₃, SrNb_{0.4}Ti_{0.6}O₃ ($t = 390$ nm) / SrTiO₃, SrNb_{0.4}Ti_{0.6}O₃ ($t = 200$ nm) / SrNb_{0.2}Ti_{0.8}O₃ ($t = 220$ nm) / SrTiO₃, SrNb_{0.2}Ti_{0.8}O₃ ($t = 220$ nm) / SrNb_{0.4}Ti_{0.6}O₃ ($t = 200$ nm) / SrTiO₃ samples. (c) Polarization dependent near edge X-ray absorption fine structure (NEXAFS) analysis for SrNb_{0.2}Ti_{0.8}O₃ (400 nm) / SrTiO₃, SrNb_{0.2}Ti_{0.8}O₃ (400 nm) / LaAlO₃ and SrNb_{0.4}Ti_{0.6}O₃ (400 nm) / SrTiO₃.

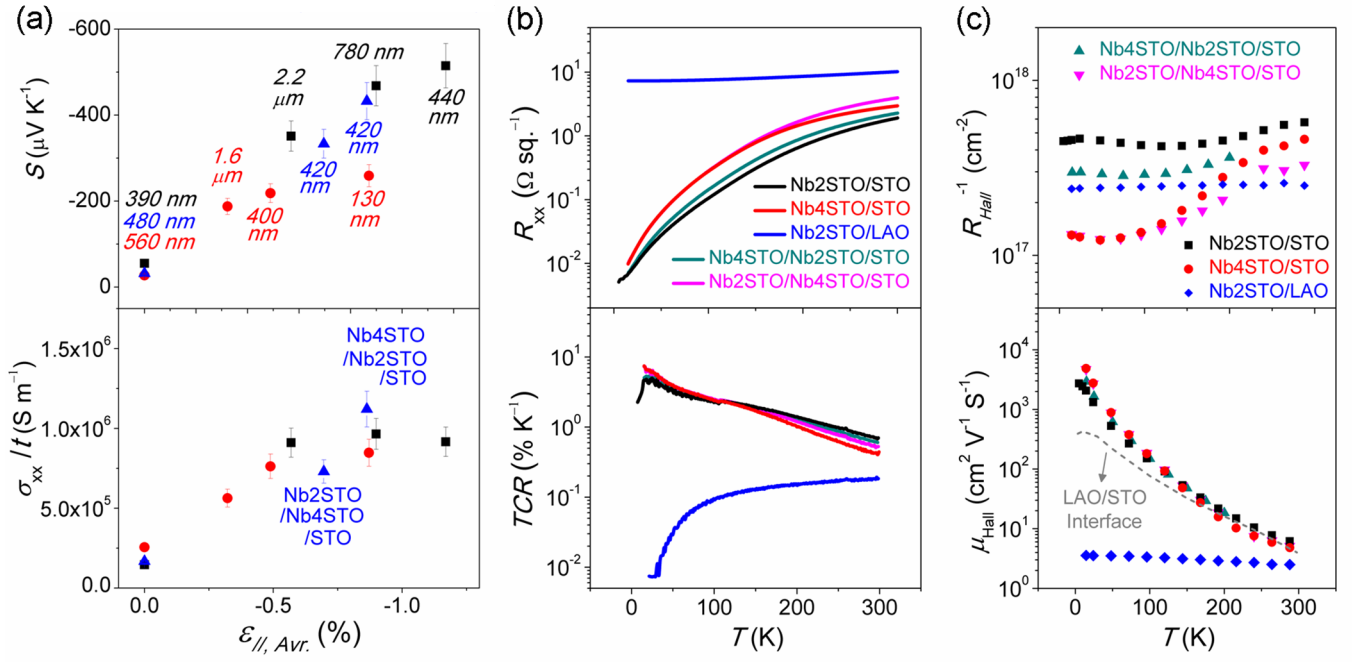


Figure 2. (a) Seebeck coefficient (S) and sheet conductance (σ_{xx}) divided by deposition thickness (t) for SrNb_xTi_{1-x}O₃ film samples at different lattice distortion ($\epsilon_{//, Avr.}$). (b) The sheet resistance (R_{xx}) and temperature coefficient of resistance (TCR), (c) sheet carrier concentration (R_{Hall}^{-1}) and Hall mobility (μ_{Hall}) for several representative SrNb_xTi_{1-x}O₃ film samples measured as a function of temperature from 5-300 K.

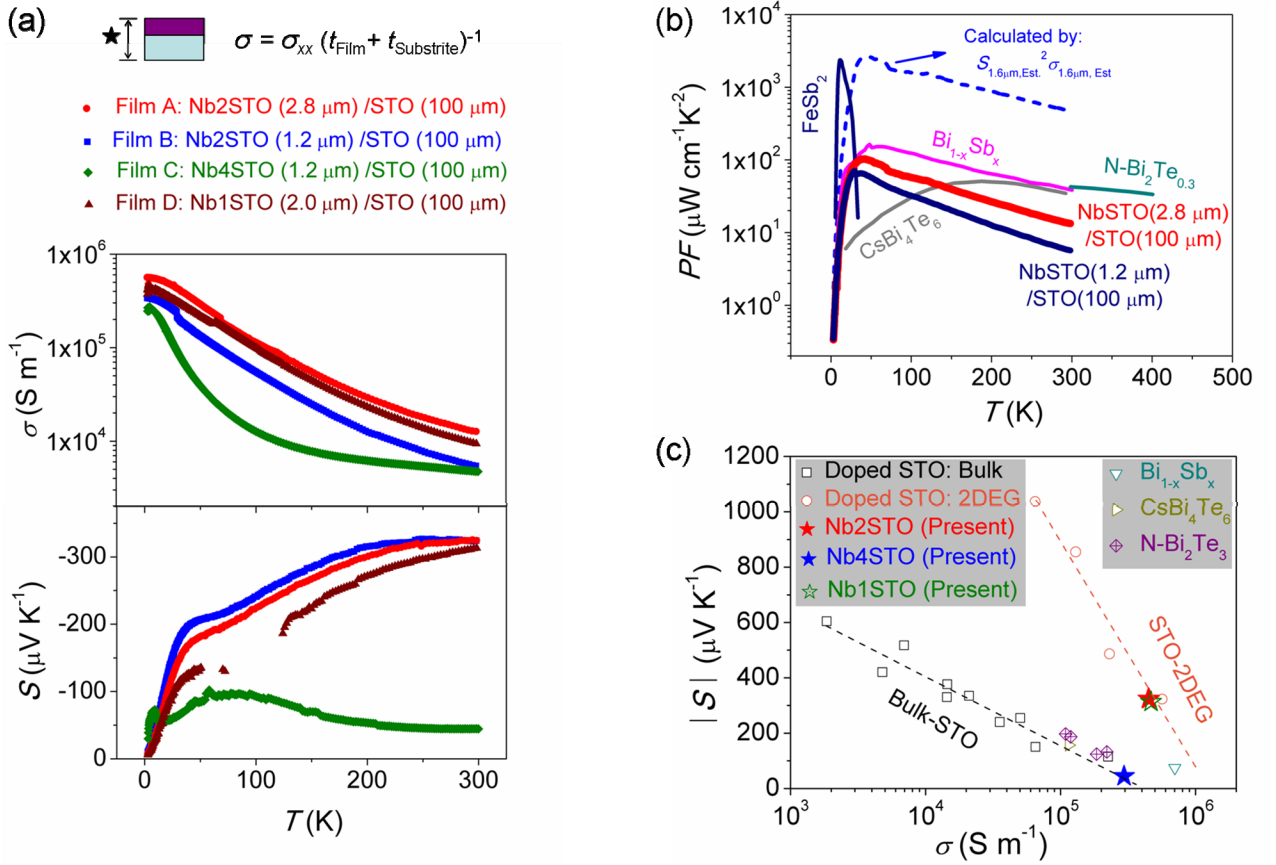


Figure 3. (a) Temperature dependence of electrical conductivity (σ) and Seebeck coefficient (S) for the following four samples: A. $\text{SrNb}_{0.2}\text{Ti}_{0.8}\text{O}_3$ ($t = 1.2 \mu\text{m}$) / SrTiO_3 ($t = 100 \mu\text{m}$), B. $\text{SrNb}_{0.2}\text{Ti}_{0.8}\text{O}_3$ ($t = 2.8 \mu\text{m}$) / SrTiO_3 ($t = 100 \mu\text{m}$), C. $\text{SrNb}_{0.4}\text{Ti}_{0.6}\text{O}_3$ ($t = 1.6 \mu\text{m}$) / SrTiO_3 ($t = 100 \mu\text{m}$), and D. $\text{SrNb}_{0.1}\text{Ti}_{0.9}\text{O}_3$ ($t = 2 \mu\text{m}$) / SrTiO_3 ($t = 100 \mu\text{m}$). As-shown σ as is calculated by sheet conductivity divided by the sum-up thickness of the film and substrate (as a bulk material). (b) Thermoelectric power factor (PF) for sample A-D. Even taking the substrate into account, as achieved maximum PF for $\text{SrNb}_{0.2}\text{Ti}_{0.8}\text{O}_3$ (2.8 μm) / SrTiO_3 (100 μm) reaches to $\sim 103 \mu\text{W m}^{-1} \text{K}^{-2}$, which is the highest value among the oxide thermoelectric bulk material [35-37]. (c) S - σ correlations for above samples compared with the ones reported for 2DEG and bulk thermoelectric materials [23-26, 35-37].

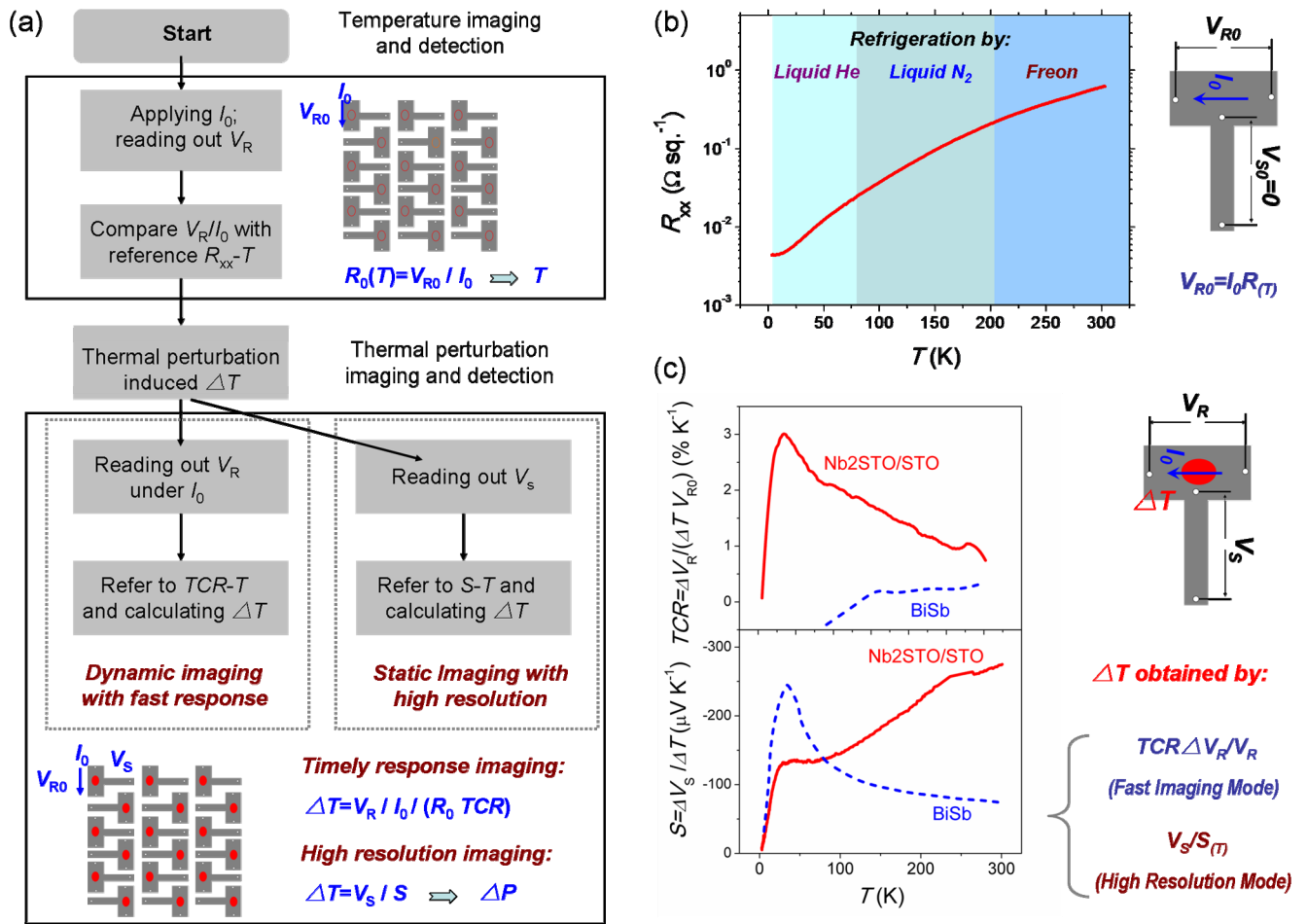


Figure 4. (a) The flow chart of the detection strategy as Joule sensor for detections of temperatures and thermal perturbations when combining the thermistor and thermoelectric functionalities. Representative temperature dependence in (b) sheet resistance, (c) temperature coefficient of resistance and Seebeck coefficient achieved in the presently grown $\text{SrNb}_x\text{Ti}_{1-x}\text{O}_3/\text{SrTiO}_3$ compared to conventional low temperature thermoelectric material of BiSb^[36].